Australian Government
Department of Defence
Defence Science and
Technology Organisation

Sea-Spike Detection in High Grazing Angle X-band Sea-Clutter

Luke Rosenberg

Electronic Warfare and Radar Division

Defence Science and Technology Organisation

DSTO–TR–2820

ABSTRACT

Knowledge of radar sea-clutter phenomenology allows accurate models to be developed for assessing target detection performance. The majority of work in this area has been at low-grazing angles from clifftops or wave tanks and does not consider scattering in the high grazing angle region beyond 10°. To improve our understanding at high grazing angles 15° to 45°, the DSTO's Ingara airborne X-band fully polarimetric radar has been used to collect 12 days worth of sea-clutter data. This report focuses on understanding the characteristics of sea-spikes as they are often the cause of false detections in a radar processor. Using the Ingara data, a threshold is used to isolate these scatterers in the range/time domain with results verified against the KK probability distribution function. Detections due to discrete and persistent scattering are then isolated to provide more information regarding the underlying cause of sea-spikes and answer the question of whether Walker's three component mean Doppler spectrum model is suitable at high grazing angles.

Published by

DSTO Defence Science and Technology Organisation
PO Box 1500
Edinburgh, South Australia 5111, Australia

Telephone: (08) 7389 5555
Facsimile: (08) 7389 6567

AR No. 015-571
April 2012

APPROVED FOR PUBLIC RELEASE

Sea-Spike Detection in High Grazing Angle X-band Sea-Clutter

Executive Summary

This report builds on work undertaken at the Defence Science and Technology Organisation (DSTO) in characterising the maritime environment from high altitude airborne platforms. Traditionally, maritime surveillance of small targets is conducted from low altitude platforms and hence with low grazing angles. This surveillance scenario has been well studied and relevant models have been developed. However, little data has been collected and analysed from the high grazing angles typically expected with the operation of high altitude airborne platforms. In August 2004 and July 2006, the DSTO's Ingara X-band airborne radar collected fine resolution fully polarimetric data in the high grazing angle region, $15^\circ - 45^\circ$. The data was collected in the ocean off the coasts of Port Lincoln and Darwin respectively.

This report investigates the detection and characterisation of sea-spikes which result from non-Bragg scattering with the goal of being able to better distinguish them from targets of interest. The approach taken is to threshold the magnitude of the raw backscatter data in the range/time domain. The percentage of sea-spikes present in the data is then measured. Results show that the majority occur in the lower grazing angle region for the horizontal transmit, horizontal receive (HH) channel and are slightly higher in the cross wind directions for the horizontal transmit, vertical receive (HV) and vertical transmit, vertical receive (VV) channels. These results are verified by comparing the trends with a separate analysis which used the KK probability distribution function (PDF) to model the sea-clutter.

An image processing algorithm is then used to isolate the discrete and persistent scatterers and test whether Walker's mean Doppler spectrum model is valid with the higher grazing angles. The results show that the persistent 'whitecaps' are spread quite evenly in grazing and azimuth for the HH channel with a clear trend in the cross-wind directions for the HV and VV channels. While there were many common peaks in both the HH and VV channels, there are however, a lot of detections present in HH but not in VV. Also, there are many discrete scatterers detected in the VV channel. This indicates that Walker's three channel model is not totally valid at high grazing angles.

THIS PAGE IS INTENTIONALLY BLANK

Author

Dr. Luke Rosenberg
Electronic Warfare and Radar Division

Luke Rosenberg received his BE (Elec.) with Honours from Adelaide University in 1999 and joined DSTO in January 2000. Since this time he has completed both a Masters degree in signal and information processing and a PhD in multichannel synthetic aperture radar through Adelaide University. He has worked at the DSTO as an RF engineer in the Missile Simulation Centre, as a Research Scientist in the imaging radar systems group and now in the Maritime Radar Group. Current research interests include radar and clutter modelling, adaptive filtering and radar detection theory.

THIS PAGE IS INTENTIONALLY BLANK

Contents

Figures

Tables

1 Introduction

In August 2004 and July 2006, the DSTO Ingara X-band airborne Synthetic Aperture Radar (SAR) collected fine resolution dual and fully polarimetric data over the high grazing angle region, 15° to 45°. This report builds on work undertaken at the DSTO to understand the characteristics of sea-clutter in order to validate existing and formulate new statistical models for the sea-clutter. These studies have included the mean backscatter, amplitude statistics and the mean Doppler spectrum [Crisp et al. 2008, Dong 2006, Rosenberg, Crisp & Stacy 2010, Rosenberg & Stacy 2008, Rosenberg, Crisp & Stacy 2008]. This report focuses on the detection and characterisation of the sea-spike component of sea-clutter with the goal of being able to better distinguish them from targets of interest.

There are three main methods of characterising the sea-spike component of the sea-clutter. The first is to apply a threshold to the data in order to distinguish between Bragg scattering and sea-spike events [Jessup, Melville & Keller 1991, Liu & Frasier 1998, Melief et al. 2006, Walker 2001*b*]. This is done without any assumption about the underlying statistics. The second and third methods fit relevant models to the PDF and the mean Doppler spectrum respectively, [Dong 2006, Rosenberg, Crisp & Stacy 2010, Walker 2001*a*, Rosenberg & Stacy 2008, Rosenberg, Crisp & Stacy 2008]. These models incorporate parameters to distinguish between the different scattering mechanisms present in the sea-clutter.

This report uses the first method in order to test the validity of relevant PDF and mean Doppler spectrum models. Section 2 describes the different scattering components present in sea-clutter and a review of techniques which have been applied to distinguish between them. Also included in this section is relevant background on the Ingara radar and details of the sea-clutter trials. Section 3 then presents a methodology for detecting sea-spikes with a suitable threshold. Comparisons are made with the KK PDF model [Dong 2006, Rosenberg, Crisp & Stacy 2010] as a means of verifying the results.

The most relevant mean Doppler spectrum model is based on data from low grazing angles [Walker 2001*a*]. Walker has proposed a three element model for Bragg, persistent whitecap and discrete sea-spike scattering. In this two channel model (HH and VV), the persistent whitecap components are common in both channels, while the 'discrete' sea-spike component is only present in HH. This model has been applied to the Ingara data [Rosenberg & Stacy 2008, Rosenberg, Crisp & Stacy 2008] but the question was raised whether this model was appropriate at higher grazing angles. Unfortunately, due to the low pulse repetition frequency (PRF) of the full-pol Ingara data, it is not easy to distinguish the three separate components in the Doppler spectrum. Further processing in the range/time domain is therefore applied to identify persistent sea-spikes corresponding to wave crests or 'whitecaps'. The relationship between the persistent sea-spikes and the mean Doppler spectrum is shown with a description of Walker's three component Doppler spectrum model. The new results are then used to assess the validity of this model at high grazing angles.

2 Background

There are a number of textbooks which focus on aspects of modelling sea-clutter, [Skolnik 1990, Nathanson, Reilly & Cohen 1991, Long 2001, Ward, Tough & Watts 2006]. The first two summarise early work from the 1960s and 1970s with a useful summary of sea-clutter radar cross section (RCS) values up to 60° grazing in [Nathanson, Reilly & Cohen 1991]. Long [2001] as well as discussing this early work with detailed notes on the literature, goes on to more recent work, such as [Lee et al. 1995*b*], which considers higher grazing angles.

Section 2.1 describes the different scattering components present in sea-clutter and a review of techniques which have been applied to distinguish between them. A brief description of the Ingara radar is then presented in Section 2.2 with background to the two sea-clutter trials presented in Section 2.3.

2.1 Sea-spike discrimination

Sea-clutter was originally characterised by matching experimental data with a combination of electromagnetic and rough surface scattering theory. The 'composite surface model' was originally proposed to describe this Bragg scattering theory [Wright 1968, Peake 1959]. Further research then led to hydrodynamic models which were used to explain the physical nature of the waves and showed a good match with the existing theory [Valenzuela & Laing 1970]. However, as more experimental data was collected, it was found that larger wind speeds caused waves which travelled at faster speeds than was predicted by the Bragg theory.

Over the past years, a number of authors have proposed different theories to explain the sea dynamics due to non-Bragg scattering, [Duncan, Keller & Wright 1974, Jessup, Keller & Melville 1990, Jessup, Melville & Keller 1991, Werle 1995, Lee et al. 1995*a*, Keller, Gotwols & Chapman 2002, Melief et al. 2006]. These are primarily concerned with analysis of breaking waves and understanding the main components of the associated radar response. Non-Bragg scattering is commonly represented as a single component and referred to as 'sea-spikes'. A common definition of a sea-spike is a radar return which has a large Doppler component with a wide bandwidth, strong backscatter power as well as a HH return that is equal or greater than the VV return. Lee et al. [1995*a*] summarises three possibilities to explain the phenomena which contribute to non-Bragg scattering:

- There is a wave which is about to break and has a much longer wavelength than the Bragg resonant wave.
- There is a breaking wave which has a long wavelength and large specular return.
- There is an attenuation in the VV channel due to Brewster angle damping and the HH channel is affected by multipath scattering and shadowing of the wave troughs by large crests.

Alternatively, Long [2001] has distinguished sea-spikes by their duration, with some lasting for a short time before fading rapidly and others persisting for 1-2 seconds. These second type are what are commonly mistaken for targets as they may exhibit many of the same characteristics including polarisation independence.

There have been a number of techniques proposed for discriminating between different types of scattering by thresholding the data. The first significant study was by Jessup, Melville & Keller [1991] who looked closely at the relationship between breaking waves and sea-spikes. An experiment was conducted on a platform in the Chesapeake Bay using a Ku band scatterometer with a 45° grazing angle. By analysing a 15 s block of data, the frequency spectrum was calculated every 0.25 s and the two-dimensional spectrogram was analysed. At points where breaking waves were observed, the HH to VV ratio was close to unity, the sea-spike backscatter maxima occurred close in time to local maxima in the mean Doppler frequency and the bandwidth maxima associated with the sea-spikes was delayed from the sea-spike maxima by approximately 0.25-0.5 s. After careful analysis of each wave using a video camera, it was found that 80% of the sea-spike events were typically associated with breaking waves and could be tracked for seconds in the field of view of the radar or up to 5 metres downwind of the breaking wave. A number of criteria were then used for detecting sea-spikes caused by breaking waves. These were based on an arbitrary RCS threshold applied to each polarisation channel, a threshold applied to the bandwidth and a combination of both. It was found that the latter threshold achieved a detection rate of approximately 70% with similar results for both polarisation channels.

A related study by Keller, Gotwols & Chapman [2002] used the same scatterometer as Jessup. To detect sea-spikes, they used the same combined criteria with the added conditions that the backscatter power must exceed the mean for at least a second and the Doppler bandwidth must peak within that time window. They verified their results using co-located video and looked at different grazing angles, wind speeds and directions. One interesting result from their study was that as the grazing angle decreased below 30°, the VV spikes became more common than HH.

A similar study was conducted with lower grazing angles at X-band by Liu & Frasier [1998]. They also used a video camera to distinguish between sea-spikes caused by steep sloping waves and those from breaking whitecaps. They estimated the magnitude, velocity and coherence of the dual-pol data they received for four different sea conditions. Their criteria for detecting sea-spikes is a power level 10 dB above the mean noise plus clutter level, combined with a coherence which exceeds 0.8. Their analysis also looked at the Doppler spectrum and found that the majority of sea-spikes have a HH to VV ratio above unity. They conclude that it is difficult to distinguish between the different sea-spike mechanisms and that a simpler criterion based solely on the power threshold should be sufficient to detect sea-spikes.

This was the approach taken by Melief et al. [2006] who looked at low grazing angle clifftop data and observed that the spiking events associated with breaking waves possess a HH power which is equal or higher than their power in the VV channel. By looking at the ratio of HH to VV and the Doppler frequency as a function of range and time, a threshold criterion was developed, $p > \mu + n\sigma$, where μ and σ are the the mean and standard deviation of the backscatter magnitude and n is a positive number. They found a wide spread of values in the sea-spike density as it varied with grazing, azimuth and wind speed.

Another technique is to apply a low pass filter to the data [Walker 2001*b*]. Walker demonstrated that with an appropriate choice of cutoff frequency, it is possible to separate sea-spikes from the sea-clutter. The study by Dong & Crisp [2008] has looked at the application of the Euler decomposition to high grazing angle X-band sea-clutter. They discriminated sea-spikes by taking the top 0.1% of the highest RCS reflectivity from either the HH or VV channel. Interestingly with this criterion, 98% of the sea-spikes belonged to the VV channel.

Finally, the paper by Greco, Stinco & Gini [2010] looked at identifying sea-spikes from a

fixed X-band radar for HH and VV channels independently and then combined together. Their classification metric comprises a minimum spike width of 0.1 s, a minimum interval between spikes of 0.5 s and a power criterion where the amplitude is five times the mean power of the received returns.

2.2 Radar description and pre-processing

The DSTO Ingara system is an airborne multi-mode X-band imaging radar system. It operates with a centre frequency of 10.1 GHz and supports a 600 MHz bandwidth for fine resolution in a spotlight mode. The sea-clutter trials however used a bandwidth of 200 MHz to achieve a larger swath width. The radar is fully polarimetric and utilises a dual linear polarised antenna developed by the Australian CSIRO for both transmitting and receiving [Parfitt & Nikolic 2001]. In fully polarimetric collections, the system is operated at double the normal PRF with the polarisation switch used to alternate the transmit polarisation between horizontal and vertical polarisations while receiving horizontal and vertical polarisations simultaneously. A more detailed description of the system may be found in [Stacy et al. 2003]. The standard radar operating parameters used during the sea-clutter collections are shown in Table 1. Note that the azimuth resolution is coarse since the radar is operated in a real beam mode.

Table 1: *Standard radar operating parameters for ocean backscatter collections*

Parameter	Value
Frequency	10.1 GHz
Transmitted bandwidth	200 MHz
Range / az. resolution	0.75 m / 63 m
Specified pulse separation	0.15 m
Full-pol. pulse separation	0.30 m

Before the data was analysed, a number of pre-processing steps were applied. Firstly, to avoid biasing the results, the data set was scanned to identify and remove any ‘bad’ regions. These include some transmit-off regions which were sampled and any other artifacts due to the radar collection. This was done visually and less than 1% of data was removed in this way. The raw data then goes through the processing chain shown in Figure 1. Range processing occurs in hardware as a stretch process. The sampled signal was then processed to first remove bandpass filter modulations and adjusted for motion compensation using both the inertial navigation unit and the global positioning system onboard the radar platform. The next steps included a correction for the variation in ground range resolution due to changes in grazing angle, removal of the elevation beampattern and polarimetric calibration using the procedure described in [Quegan 1994].

2.3 Trials background

The trial data was obtained with Ingara on two separate occasions and from two distinctly different regions. The first ‘sea-clutter’ trial was conducted in 2004 (SCT04) in the southern ocean approximately 100 km south of Port Lincoln, South Australia [Crisp, Stacy & Goh 2006]. The site chosen was at the edge of the South Australian continental shelf where there was little chance of shallow

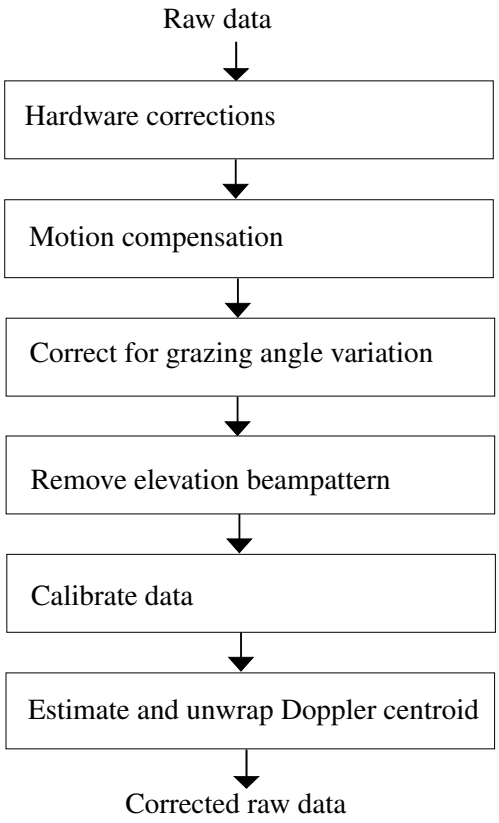

Figure 1: *Ingara pre-processing diagram*

water affecting the wave field. During the trial, ocean backscatter was collected for a range of different geometries on eight separate days with different ocean conditions. The second 'maritime surveillance' trial was conducted in 2006 (MAST06) in littoral and open sea environments near Darwin in the Northern Territory. Again, data was collected for a range of different geometries and ocean conditions. In this trial, a total of four day's data were collected: two of the days were in the littoral zone approximately 25 km north of Darwin and the other two days were in the open ocean approximately 200 km west of Darwin.

During the ocean backscatter collections, Ingara was operated in the circular spotlight-mode. Figure 2 shows the collection geometry for this mode, where the aircraft flies a circular orbit in an anti-clockwise direction (as seen from above) around a nominated point of interest, while the radar beam is continuously directed toward this point. Radar echo data is continuously collected during the full 360° orbit, with the instantaneous PRF appropriately adjusted to maintain a constant spatial pulse separation between pulse transmission positions. Once collected, the echo data may be processed either immediately (in real-time) or subsequently (off-line) to produce either range-compressed profiles or spotlight SAR images of the scene at various azimuth angles. Further, owing to the continuous nature of the data collection, the images can be formed at any desired azimuth look direction. Each collection of data in this mode is referred to as a 'run' and there may be several complete orbits in a single run.

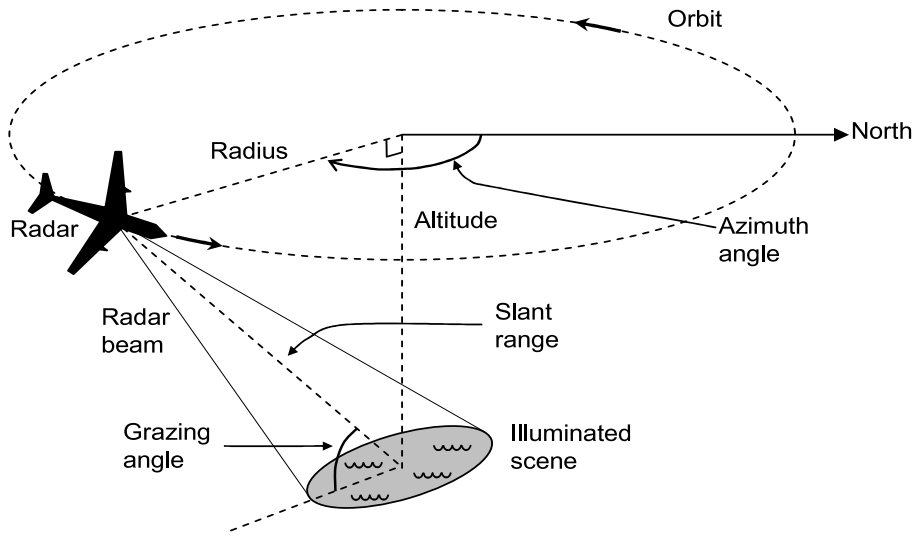

Figure 2: *Circular spotlight mode collection geometry*

In order to examine the effect of grazing angle on ocean backscatter, runs were made with different altitude and orbit diameters. For both the SCT04 and MAST06 trials, data was collected at the centre of the spotlight for the nominal grazing angles of 15° to 45° in 5° increments. Owing to the finite beam width of the radar, its footprint on the ocean surface has a significant range extent. This means that the grazing angle varies across the footprint. It follows that, with appropriate range compression and data processing, the variation in backscatter with grazing angle across the range extent of the radar beam footprint can be measured.

Note that the aircraft speed was approximately 200 knots and so a 1.5 NM orbit took approximately 3 minutes while a 1.9 NM orbit took 3.5 to 4 minutes. The total collection across all grazing angles took approximately 90 minutes. It is reasonable to assume that over such short time intervals, the ocean surface conditions are relatively unchanged and that mean backscatter variations are mostly due to the changing imaging geometry rather than changing ocean conditions. Nevertheless, it is possible that wind gusts and changes of wind strength and direction may have affected the measurements. Table 2 shows the wind and wave ground truth for the data used in this report. For the full-pol model analysis in the following sections, F35 and F9 are used as example data sets for each trial.

Table 2: *Wind and wave ground truth. Directions are "from" not "to"*

Trial	**Flight**	**Date**	**Wind**		**Wave**		
			Speed (m/s)	**Direction (°)**	**Height (m)**	**Direction (°)**	**Period (s)**
SCT04	F35	11/8/04	10.3	315	2.6	210	10.4
MAST06	F9	24/5/06	10.2	124	1.21	128	4.6

3 Sea-spike analysis

Sea-spike detection is now performed using two days from the Ingara data set, one from the southern ocean near Port Lincoln and the other in the open ocean near Darwin. These are described in Table 2 as F35 and F9 respectively. For the results in this report, the upwind direction (wind towards the radar) is rotated to 0° with the downwind direction at -180°, the crosswind directions at $\pm 90^\circ$ and any regions with poor or missing data are shown with cross-hatching (diagonal stripes).

Section 3.1 describes the percentage of sea-spikes which are measured after applying a suitable threshold. Comparison with the KK PDF model is then presented in Section 3.2. The next Section 3.3 presents a method for discriminating between the discrete and persistent sea-spikes in the sea-clutter. Further characterisation of the sea-spikes is then presented in Section 3.4. This is followed by Section 3.5 which looks at the relationship between the sea-spike components and the mean Doppler spectrum. Results from throughout this section are then used to assess the validity of Walker's three component Doppler spectrum model at high grazing angles.

3.1 Sea-spike detection

To separate the sea-spike components, each run is split into blocks covering 1 degree in grazing and 5 degrees in azimuth. Each block then has an overlap region to allow for the detection of persistent spikes which lie in the final second of the data block. Since each data block spans a different azimuth and grazing region, a weighted average was determined by the amount of the data block which falls into the defined grid. From a study of the literature, the criterion by Melief et al. [2006] was applied to the backscatter magnitude. After careful analysis of our data, a value of $n = 5$ standard deviations above the mean was chosen for the threshold. This choice clearly picked up both the discrete spikes and persistent detections. The thresholded data can then be analysed to calculate the percentage of detections against the total number of pixels in the image.

With this threshold, the false alarm rate for F35 was calculated to be 2.8×10^{-3}, 8.1×10^{-4} and 3.8×10^{-4} for the HH, HV and VV channels respectively. Similarly for F9, the false alarm rate was calculated as 2.5×10^{-3}, 7.9×10^{-4} and 3.1×10^{-4}. The first result in Figure 3 shows the percentage of sea-spike detections against the total number of points. For both data sets, there are more sea-spike detections in the HH channel than the VV and the majority of sea-spike detections occur in the lower grazing angle region for the HH channel. They are also slightly higher in the crosswind directions for the other two polarisation channels. Other minor differences are due to the different sea conditions.

3.2 Probability distribution

Statistical models of the magnitude PDF are used to model the spread of received backscatter values. A popular physically based model is known as the K-distribution. It comprises two components, the first is fast varying with a correlation time on the order of 10 ms and the second is a slow varying component with a correlation time on the order of seconds. The fast-varying component is associated with the small ripples on top of the slow-varying component which represents the underlying long waves or swell [Ward, Tough & Watts 2006].

It is usually presented in terms of an intensity product model combining an underlying RCS component, x, with an uncorrelated speckle component, z. Assuming analysis of baseband radar

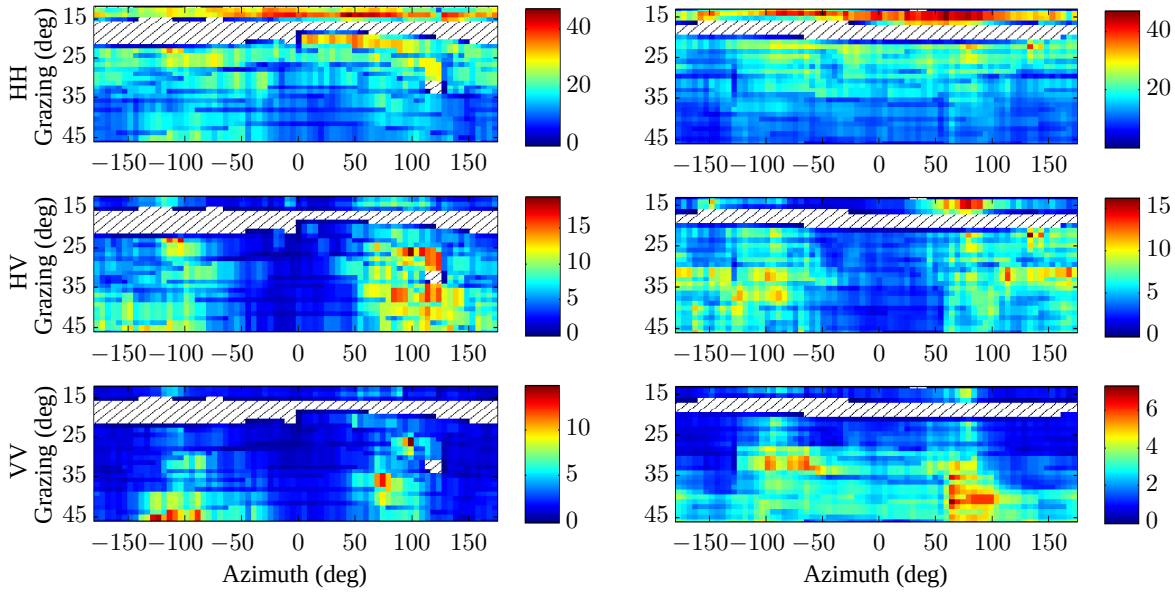

Figure 3: *Percentage of sea-spike detections for F35 (left) and F9 (right). Results are partitioned into* 1° *grazing* $\times$ 5° *azimuth blocks.*

data in complex format (in-phase and quadrature), the magnitude PDF becomes Rayleigh and the power (or intensity) PDF is modelled as an exponential (or gamma distribution with unity shape) and mean power x,

$$P_{z|x}(z|x) = \frac{1}{x}\exp\left[-\frac{z}{x}\right], \qquad z \geq 0 \tag{1}$$

In the K-distribution model, the underlying RCS, x is also a random variable and can be modelled as a Gamma distribution,

$$P_x(x|\nu,\mu) = \frac{b^\nu}{\Gamma(\nu)}x^{\nu-1}\exp\left[-bx\right], \qquad 0 \leq x \leq \infty \tag{2}$$

where ν is the shape, μ is the mean and $b = \nu/\mu$ is the scale. The compound formulation for the K-distribution is then obtained by integrating the speckle PDF over the PDF of the underlying RCS,

$$P(z|\nu,\mu) = \int_0^\infty P_{z|x}(z|x)P_x(x|\nu,\mu)dx. \tag{3}$$

From an airborne platform and with higher radar resolution, the effects from breaking waves and discrete sea-spike returns will have a significant impact on the radar backscatter with the observed PDF deviating significantly from the K-distribution model, [Ward, Tough & Watts 2006]. An alternative model which captures the high valued backscatter associated with the sea-spike component is the KK-distribution [Dong 2006]. To form the KK-distribution, the underlying RCS is represented as the sum of two scaled Gamma functions,

$$Q_x(x|\cdot) = (1-k)P_x(x|\nu_1,\mu_1) + kP_x(x|\nu_2,\mu_2) \tag{4}$$

where k is the ratio between the two components. By replacing $P_x(\cdot)$ with $Q_x(\cdot)$ in Equation 3, the result is two instances of the K-distribution mixed together, one associated with the Bragg

component and one for the sea-spikes,

$$Q(z|\cdot) = (1-k)P(z|\nu_1,\mu_1) + kP(z|\nu_2,\mu_2). \quad (5)$$

With this distribution there are now 5 parameters to be determined. This can be reduced to 2 however, by setting the mean of the first component to the overall mean of the distribution and by setting both of the underlying shape parameters to be the same. Then by fixing the ratio between components at $k \equiv 0.01$, the ratio of means, ρ can be used as the sole measure of separation between the KK components.

In the previous study [Rosenberg, Crisp & Stacy 2010], these parameters were determined by fitting the KK model to the data histogram using the 'Levenberg-Marquardt' algorithm. Figure 4 shows an example PDF for the HH channel with fits for the K and KK distributions. In this figure, the K distribution does not model the tail of the data below 10^{-3}, while the KK matches very closely. The result in Figure 5 then shows that the KK ratio of means has similar trends to Figure 3 for both data sets.

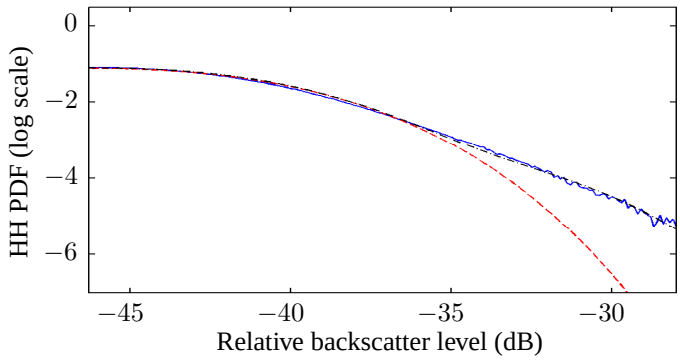

Figure 4: *PDF example: (—) data, (- -) K, (-.-) KK*

3.3 Persistent and discrete detections

Detection of the persistent sea-spikes / whitecaps is essentially a line detection procedure in the range/time domain. Each line then corresponds to a breaking wave which can be used to quantify the number of persistent sea-spikes. As a caveat to these results, there is no visual verification or ground truth in which to compare.

The algorithm used is based on a number of image processing techniques outlined in Figure 6. The first stage is to horizontally dilate the thresholded data to join up any closely spaced points with the amount of dilation determined through visual inspection to ensure that the dominant waves were detected. The second stage then removes any unconnected detections which are assumed to not correspond to whitecaps. The third stage is to use a Hough transform to transform the data into a space described by lines with a given length and angle. Only lines with angles within $\pm 10°$ relative to the horizontal are considered for this transform which corresponds to a maximum radial velocity of 57.9 m/s[1] when the correct scaling is applied to the slope. The strongest points in this domain then correspond to the dominant lines in the image and a threshold is applied to isolate these. An inverse Hough transform then reveals the dominant lines present in the original image.

[1]The corresponding maximum Doppler frequency is 3.9 kHz.

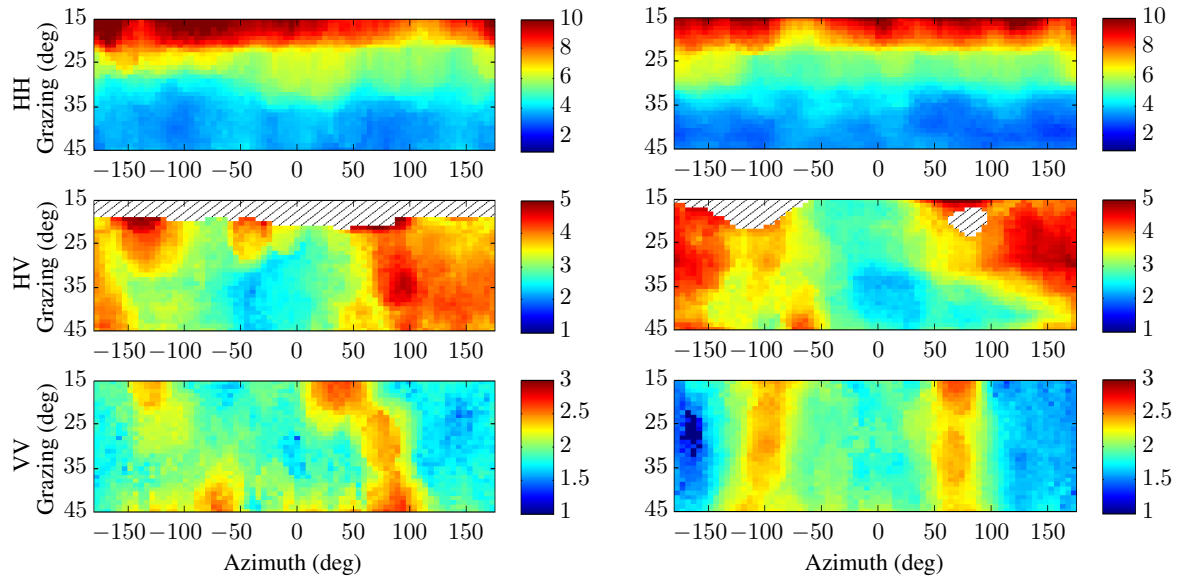

Figure 5: *Ratio of means (ρ) from the KK-distribution for F35 (left) and F9 (right). Results are partitioned into* 1° *grazing* $\times$ 5° *azimuth blocks.*

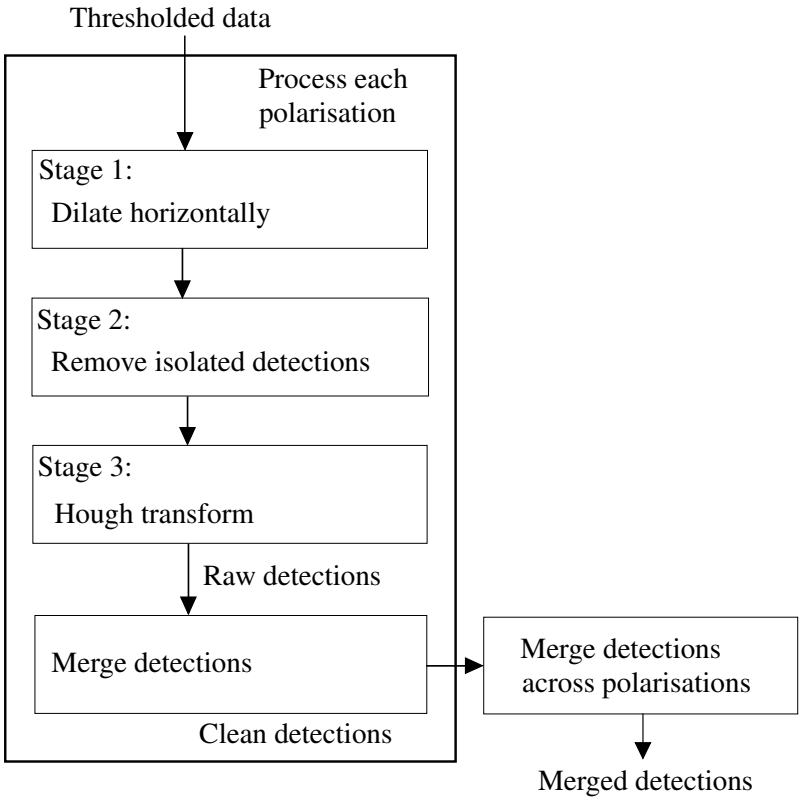

Figure 6: *Line detection algorithm overview*

Figure 7 shows an example of a thresholded image, a dilated image and the image after the removal of the unconnected blocks. The dominant lines are then highlighted in Figure 8. Close examination reveals that often there is more than one dominant line for each whitecap and many of the lines overlap with different slope. A further processing stage is therefore required to merge these lines and isolate whitecaps. Two criteria are used for this process: lines which either lie close together or have end points within 0.05° in grazing and 0.5 s in time and any lines which overlap. Finally, to ensure the persistency of whitecaps, only detections which last for at least 1 s are retained. These clean detections are highlighted in Figure 9. The final stage is to consider the three polarisation channels together. All whitecap detections found in more than one channel are merged together and the location of all whitecap detections are placed in the common channels. These are highlighted in Figure 10.

As an example, consider the detected whitecap at 28° grazing on the far right of Fig. 10. In the HV and VV channels of Fig. 8, there are multiple detections which correspond to this whitecap. For the cleaned image in Fig. 8, the HH and HV channels have removed the smaller whitecaps as their time extent is less than 1 s, while in the VV channel, the lines have been connected to represent a single whitecap. Then in Fig. 10, the extended whitecap is present in each polarisation channel and is the same length.

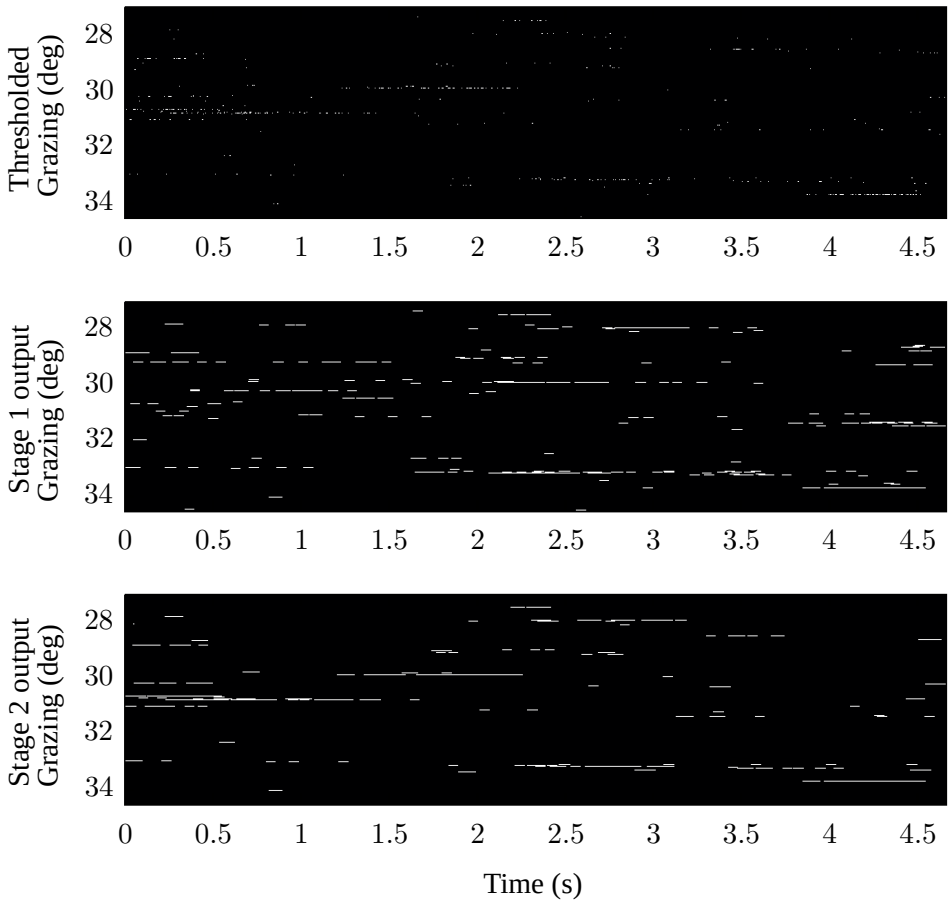

Figure 7: *Thresholded data and line detection example stages 1 and 2*

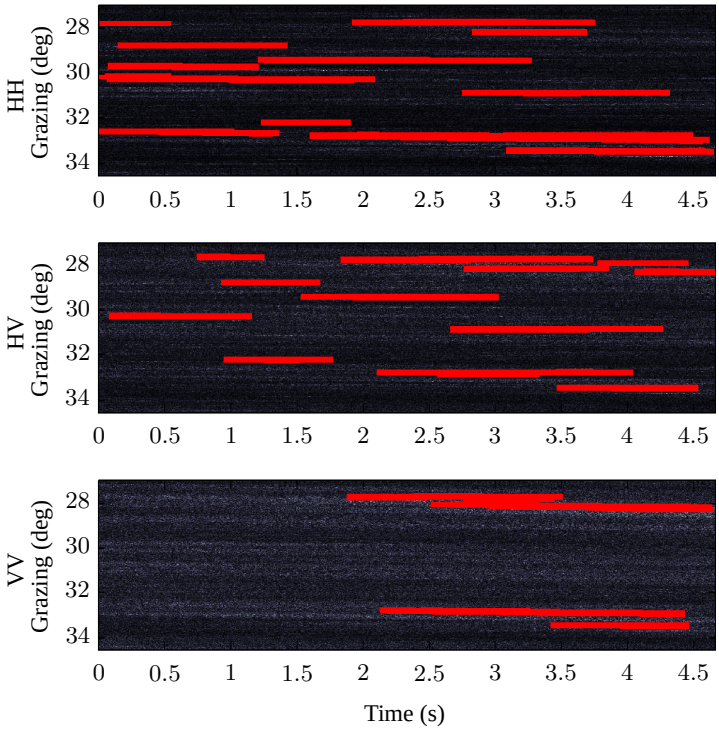

Figure 8: *Dominant line detection example*

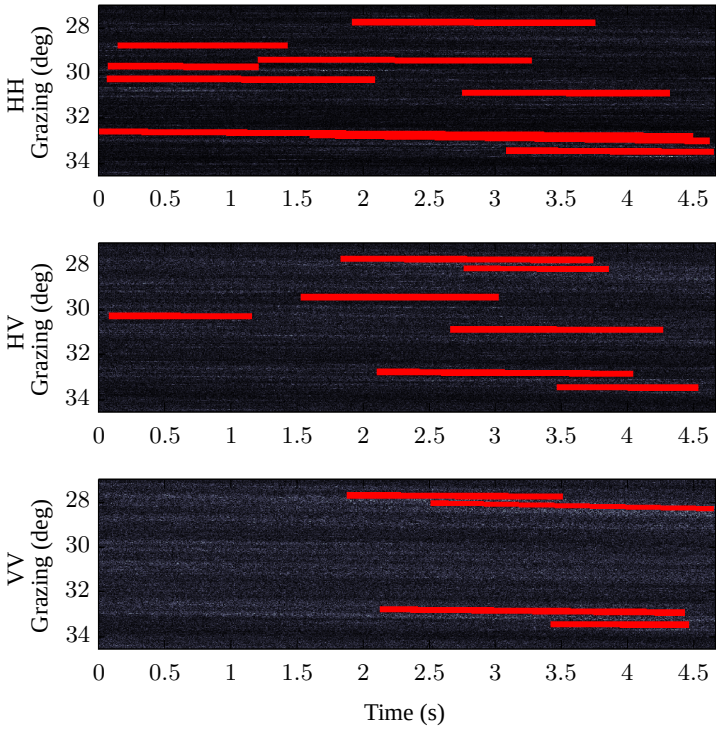

Figure 9: *Clean line detection example*

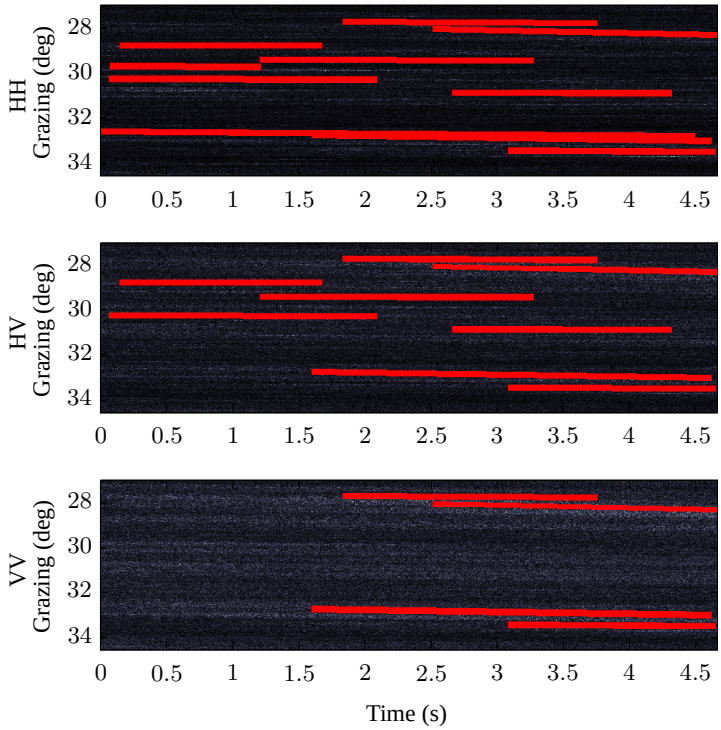

Figure 10: *Merged line detection example*

In order to separate the detections due to whitecaps, a box is drawn around the detected lines and any detections which fall in that box count towards a whitecap detection. Figure 11 shows the percentage of whitecap detections after combining detections from different polarisation channels. The result shows that the whitecaps are spread quite evenly in grazing and azimuth for the HH channel. There is also a clear trend in the cross-wind directions for the HV and VV channels where scattering from whitecaps is more dominant. Once the persistent whitecaps are isolated, it is possible to identify the remaining 'discrete' detections. These are shown in Figure 12 with the majority of detections in the crosswind directions with a small region in the lower grazing angle of HH.

A study over the other data sets revealed that the number of both persistent and whitecap detections are directly related to the sea-state. This is intuitive since clearly there are less breaking waves when the wind speed is lower. Interestingly, the main trend observed for the HH channel in the low grazing angle upwind direction is consistent across all the data sets, while the detections along the cross wind direction is only present in some of them.

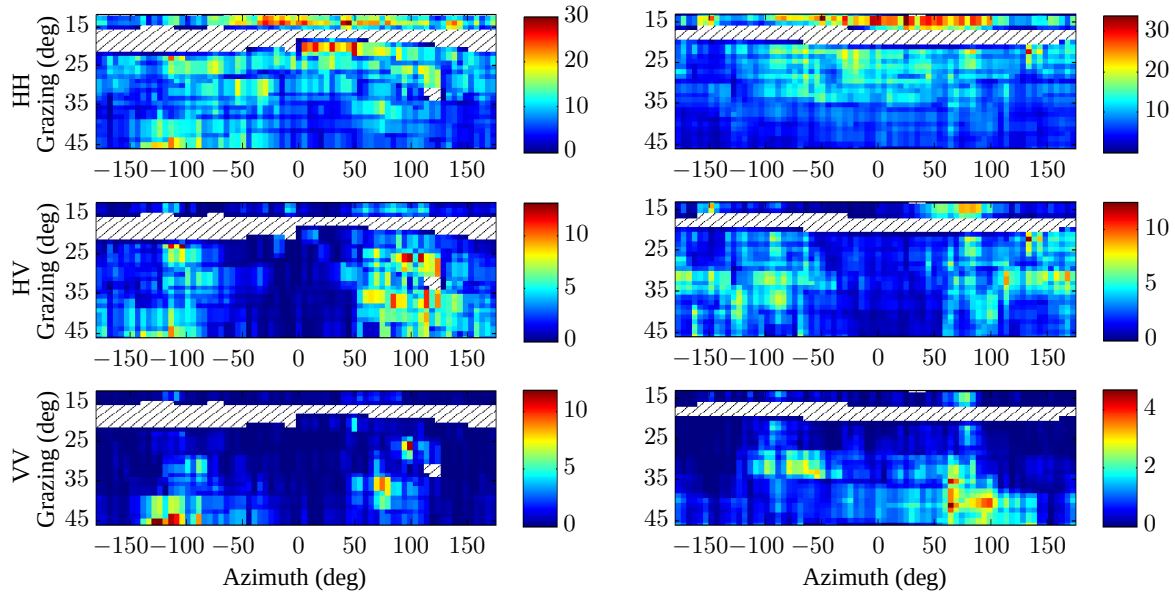

Figure 11: *Percentage of whitecap detections for F35 (left) and F9 (right). Results are partitioned into* 1° *grazing* $\times$ 5° *azimuth blocks.*

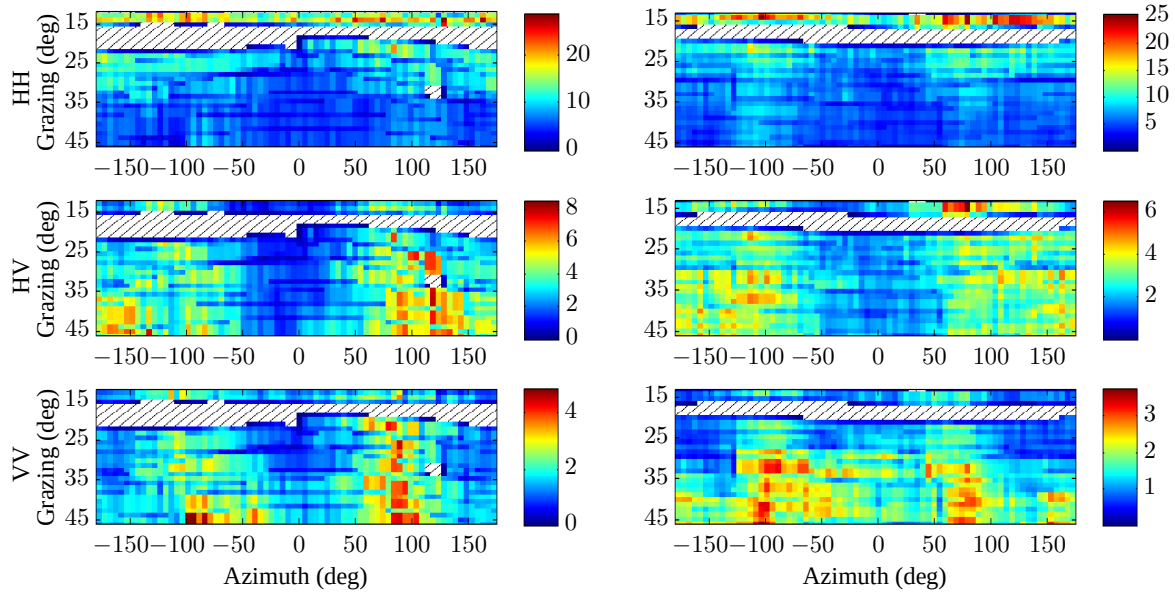

Figure 12: *Percentage of discrete sea-spike detections for F35 (left) and F9 (right). Results are partitioned into* 1° *grazing* $\times$ 5° *azimuth blocks.*

3.4 Sea-spike characteristics

To further characterise the sea-spikes, a number of parameters have been extracted from the data. The first three are the wave velocity, life time and decorrelation time. The mean values for each polarisation channel are given in Tables 3-4 for the F35 and F9 data sets, with their PDFs shown in Figures 13-14.

The absolute wave velocity and life times are determined from the slope and time extent of the waves in the range/time domain respectively. However, the wave velocity is measured in the radial direction v_{r} which will vary as the radar look direction / azimuth angle θ_{az} varies. To obtain the true wave velocity v_{w}, this radial velocity needs to be projected along the wave direction θ_{w},

$$v_{\mathrm{w}} = v_{\mathrm{r}} \cos(\theta_{\mathrm{az}} - \theta_{\mathrm{w}}). \tag{6}$$

The PDFs both resemble a negative exponential distribution with little change over polarisation. The mean values are between 2-3 m/s which is significantly less than the measured wind speed for these two days.

The wave life time varies from 1 to 5 s with a negative exponential decay observed for the HH and HV channels with a mean of approximately 2 s. For the VV channel, there is a more uniform spread. The autocorrelation function (ACF) is related to the mean Doppler spectrum through a Fourier transform and will in general be complex. The temporal decorrelation is measured at the point where the absolute value of the ACF decays to $1/e$. This parameter is important as it is commonly used to quantify the level of temporal correlation present in the observed sea-clutter. The mean values vary between 3.9 to 4.5 ms with little difference between polarisations. Note that these values do not account for the broadening of the Doppler spectrum due to the moving radar platform and hence the true wave decorrelation times will be slightly longer. This is not expected to be significant however as the spikes are only present in a small region of the beam.

The next results in Figures 15-16 show the PDFs for the discrete and persistent scatterers. The mean values reveal that there is little difference between the magnitudes of the two scattering types. The VV channel has the largest value, followed by HH and then HV. Between the two data sets, the mean levels vary up to 3 dB for the HH channel, while the VV channel differs by 0.6 dB.

Table 3: *F35 sea-spike characteristic means*

	HH	HV	VV
Velocity (m/s)	2.80	2.29	2.96
Life time (s)	2.02	2.12	2.53
Decorrelation time (ms)	4.49	4.49	4.25
Discrete magnitude (dB)	-15.73	-25.76	-10.77
Persistent magnitude (dB)	-15.43	-25.31	-10.60

Table 4: *F9 sea-spike characteristic means*

	HH	HV	VV
Velocity (m/s)	2.14	2.26	3.37
Life time (s)	1.98	2.14	2.54
Decorrelation time (ms)	4.31	4.12	3.87
Discrete magnitude (dB)	-12.57	-23.40	-10.18
Persistent magnitude (dB)	-12.54	-23.13	-9.97

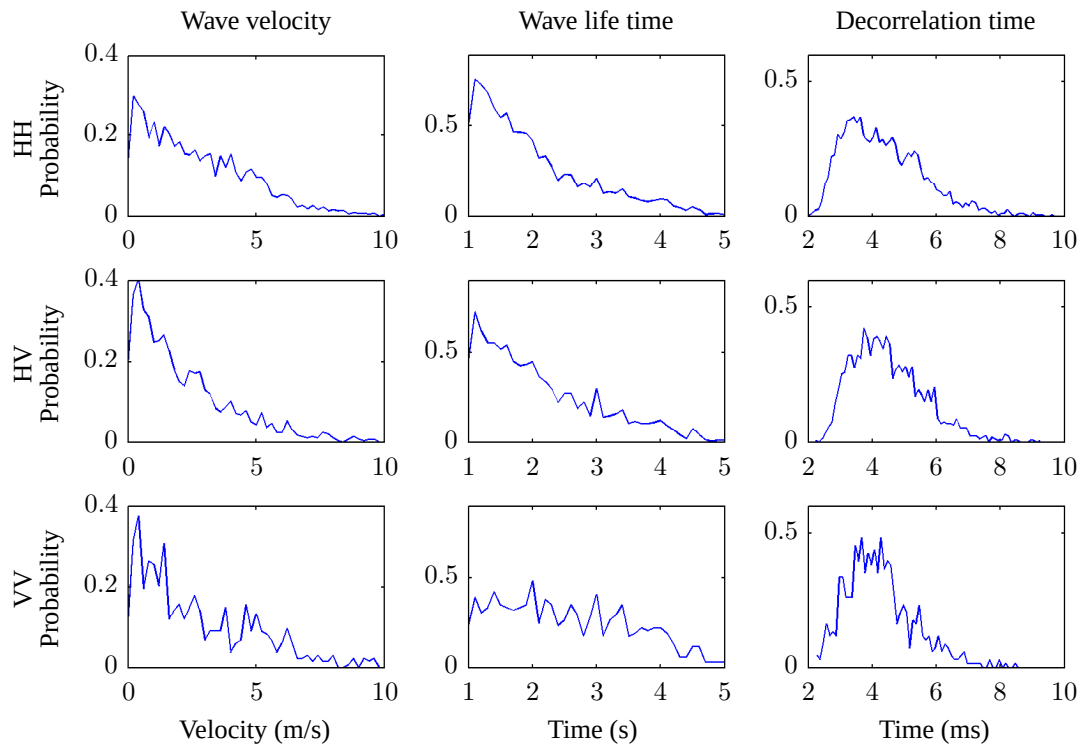

Figure 13: *F35 sea-spike characteristic PDFs - wave velocity, life time and decorrelation time*

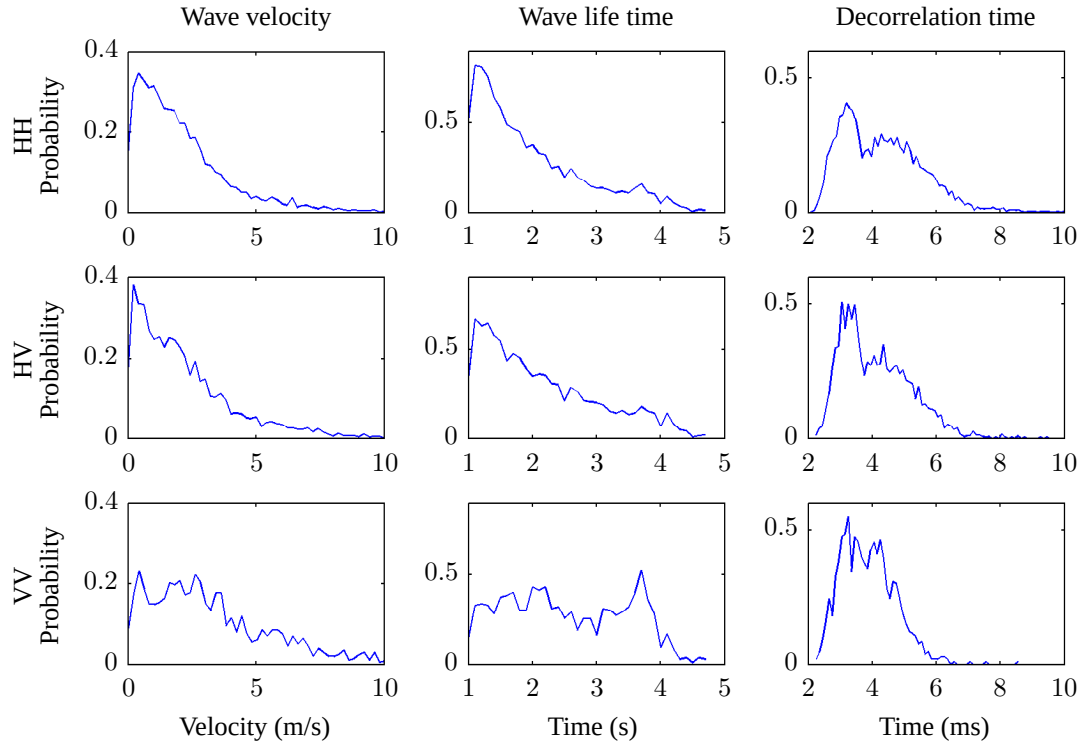

Figure 14: *F9 sea-spike characteristic PDFs - wave velocity, life time and decorrelation time*

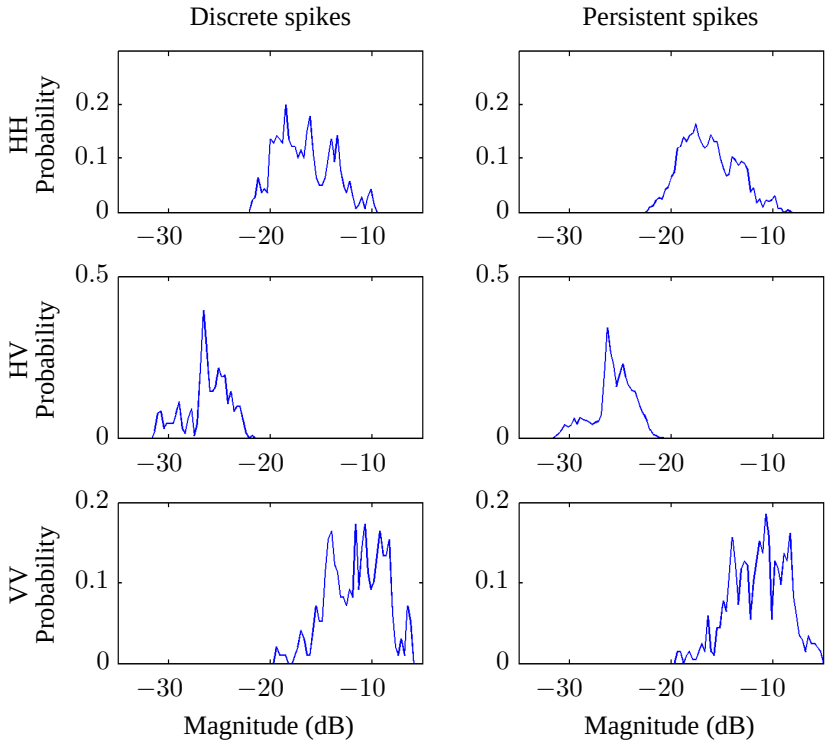

Figure 15: *F35 sea-spike characteristic PDFs - persistent and discrete magnitudes*

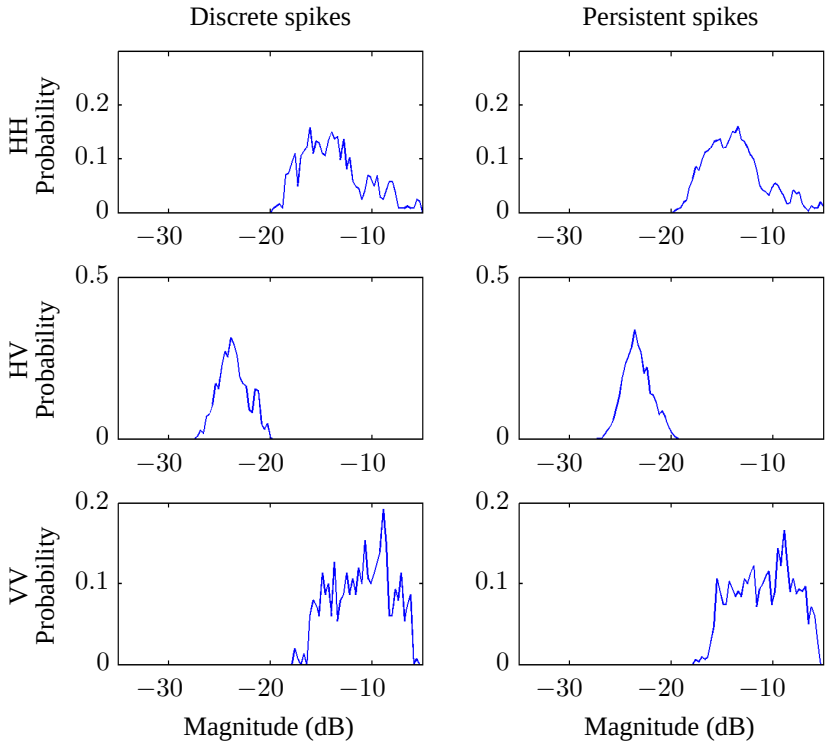

Figure 16: *F35 sea-spike characteristic PDFs - persistent and discrete magnitudes*

3.5 Doppler spectrum

A dual-pol run from the F9 dataset is now used to demonstrate the relationship between persistent sea-spikes and the Doppler spectrum. The data is collected over two consecutive runs and it is therefore assumed that the combined mean Doppler spectrum is representative of an equivalent full-pol system with a higher PRF of 600 Hz. To form the final Doppler spectrum, it must first be unwrapped using an estimate of the Doppler centroid. However due to uncertainties in the motion compensation, the absolute Doppler origin is not known. Therefore to ensure the correct separation between channels, the VV channel is centred at the Doppler origin and the HH and HV channels are shifted by the difference between HH and VV and HV and VV respectively.

Figure 17 shows a whitecap selected from the upwind direction of the HH channel spanning 3 s in time and 10 range bins. The middle plot shows its Doppler spectrum over the 10 range bins and the bottom plot shows the mean Doppler spectrum. To highlight the sea-spike, the mean Doppler spectrum of the entire data block has been plotted as a comparison[2]. The sea-spike component can then be seen at a higher frequency than the overall mean spectrum. Clearly, there are at least two components which can be isolated and therefore modelled.

Walker's mean Doppler spectrum model [Walker 2001*a*], consists of three types of scattering referred to as 'Bragg', 'whitecap' and discrete 'sea-spike events'. He models each of these scattering types with Gaussian lineshapes with the overall spectrum for each polarisation consisting of a linear combination of these components. The Bragg scattering component is formed by small ripples on top of the longer ocean waves, causing the VV polarisation to have a greater amplitude than HH, while the whitecap component is associated with the rough whitecaps formed at sea and have a weaker polarisation dependence. Walker reports that at low grazing angles this component is noticeably stronger than the Bragg scattering, particularly in HH. Sea-spikes are associated with the crest of waves and are virtually non-existent in the VV spectrum. They last for a much shorter period of time than the other returns and are coherent over that time.

Referring to Figure 11 which relates to the persistent scatterers or whitecaps, there are many common peaks in both the HH and VV channels, with a lot of detections present in HH but not in VV. This result shows that there are common components in both channels. However, there are also many extra whitecaps detected in the HH channel. Figure 12 also demonstrates that there are many discrete scatterers in the VV channel. As a result, the two assumptions that the whitecap component is identical in both HH and VV and that discrete scatterers from the VV channel are negligent are not correct. Hence Walker's mean Doppler spectrum model is not accurate at these grazing angles.

[2]Note that the Doppler spectrum has been spread due to the azimuth beampattern of the moving radar platform.

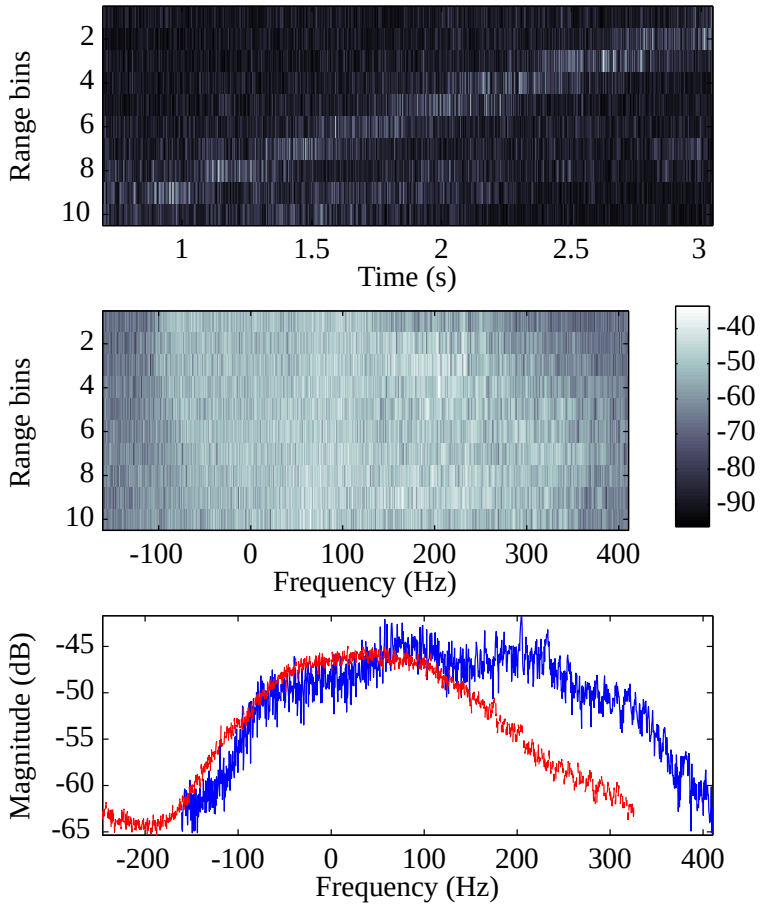

Figure 17: *Dual-pol sea-spike example, top - time domain, middle - Doppler spectrum, bottom - mean Doppler spectrum: (—) whitecap, (- -) entire block*

4 Conclusion

This report has investigated the detection and characterisation of sea-spikes with the goal of being able to better distinguish them from targets of interest. The approach used was to threshold the magnitude of the raw backscatter data in the range/time domain. The first result looked at the percentage of sea-spikes present in the Ingara high grazing angle sea-clutter data. The results showed that the majority occur in the lower grazing angle region for the HH channel and were slightly higher in the cross wind directions for the other two polarisation channels. These results were then verified by comparing the trends with a separate analysis which used the KK PDF to model the sea-clutter.

An image processing algorithm was then used to isolate the discrete and persistent scatterers and test whether Walker's mean Doppler spectrum model was valid with the higher grazing angles. The results found that the whitecaps were spread quite evenly in grazing and azimuth for the HH channel with a clear trend in the cross-wind directions for the HV and VV channels. While there were many common peaks in both the HH and VV channels, there were however, a lot of detections present in HH but not in VV. There were also many discrete scatterers detected in the VV channel. This indicates that Walker's three channel model is not totally valid at high grazing angles. Future work will look at a modified model to represent the mean Doppler spectrum at high grazing angles and how these new results can be used to improve target detection in the maritime environment.

References

Blacknell, D. & Tough, R. J. A. (2001) Parameter estimation for the K-distribution based on [z log(z)], *IEE Proceedings of Radar, Sonar and Navigation* **148**(6), 309–312.

Crisp, D. J., Kyprianou, R., Rosenberg, L. & Stacy, N. J. (2008) Modelling X-band sea clutter at moderate grazing angles, *in IEEE International Radar Conference*, pp. 596–601.

Crisp, D. J., Stacy, N. J. & Goh, A. S. (2006) *Ingara Medium-High Incidence Angle Polarimetric Sea Clutter Measurements and Analysis*, Technical Report DSTO-TR-1818, DSTO.

Departent of Defence, Australia (2012) Air 7000 project description. http://www.defence.gov.au/capability/AIR7000/.

Dong, Y. (2006) *Distribution of X-Band High Resolution and High Grazing Angle Sea Clutter*, Research Report DSTO-RR-0316, DSTO.

Dong, Y. & Crisp, D. J. (2008) The Euler decomposition and its application to sea clutter analysis, *in IEEE International radar conference*.

Duncan, J. R., Keller, W. C. & Wright, J. W. (1974) Fetch and wind speed dependence of doppler spectra, *Radio Science* **9**, 809–819.

Greco, M., Stinco, P. & Gini, F. (2010) Identification and analysis of sea radar clutter spikes, *IET Journal of Radar, Sonar and Navigation* **4**(2), 239–250.

Jessup, A. T., Keller, W. C. & Melville, W. K. (1990) Measurement of sea spikes in microwave backscatter at moderate incidence, *Journal of Geophysical Research* **95**(C6), 9679–9688.

Jessup, A. T., Melville, W. K. & Keller, W. C. (1991) Breaking waves affecting microwave backscatter, 1. detection and verification, *Journal of Geophysical Research* **96**(C11), 20,547–20,559.

Keller, M. R., Gotwols, B. L. & Chapman, R. D. (2002) Multiple sea spike definitions: reducing the clutter, *in IEEE International Geoscience and Remote Sensing Symposium*, pp. 940–942.

Lee, P. H. Y., Barter, J. D., Beach, K. L., Hindman, C. L., Lake, B. M., Rungaldier, H., Shelton, J. C., Williams, A. B., Yee, R. & Yuen, H. C. (1995*a*) X-band microwave backscattering from ocean waves, *Journal of Geophysical Research* **100**(C2), 2591–2611.

Lee, P. H. Y., Barter, J. D., Caponi, E., Hidman, C. L., Lake, B. M., Rungaldier, H. & Shelton, J. C. (1995*b*) Power spectral lineshapes of microwave radiation backscattered from sea surfaces at small grazing angles, *IEE Proceedings of Radar, Sonar and Navigation* **142**(5), 252–258.

Liu, L. & Frasier, S. J. (1998) Measurement and classification of low-grazing-angle radar sea spikes, *IEEE Transactions on Antennas and Propagation* **46**(1), 27–40.

Long, M. W. (2001) *Radar Reflectivity of Land and Sea - Third Edition*, Artech House.

Melief, H. W., Greidanus, H., van Genderen, P. & Hoogeboom, P. (2006) Analysis of sea spikes in radar sea clutter data, *IEEE Transactions on Geoscience and Remote Sensing* **44**(4), 985–993.

Nathanson, F. E., Reilly, J. P. & Cohen, M. N. (1991) *Radar Design Principles - Second Edition*, McGraw-Hill.

Parfitt, A. & Nikolic, N. (2001) A dual-polarised wideband planar array for X-band synthetic aperture radar, *in IEEE Antennas and Propagation Society International Symposium*, Vol. 2, pp. 464–467.

Peake, W. H. (1959) Theory of radar return from terrain, *in IRE Convention Record*, pp. 27–41.

Quegan, S. (1994) Unified algorithm for phase and cross-talk calibration of polarimetric data: Theory and observations, *IEEE Transactions on Geoscience and Remote Sensing* **32**(1), 89–99.

Rosenberg, L., Crisp, D. J. & Stacy, N. J. (2008) Characterisation of low-PRF X-band sea-clutter Doppler spectra, *in IEEE International Radar Conference*, pp. 100–105.

Rosenberg, L., Crisp, D. J. & Stacy, N. J. (2010) Analysis of the KK-distribution with medium grazing angle sea-clutter, *IET Proceedings of Radar Sonar and Navigation* **4**(2), 209–222.

Rosenberg, L. & Stacy, N. J. (2008) Analysis of medium angle X-band sea-clutter Doppler spectra, *in IEEE Radarcon Conference*.

Skolnik, M. I. (1990) *Radar Handbook*, 2 edn, McGraw-Hill.

Stacy, N. J. S., Badger, D. P., Goh, A. S., Preiss, M. & Williams, M. L. (2003) The DSTO Ingara airbone X-band SAR polarimetric upgrade: first results, *in IEEE International Geoscience and Remote Sensing Symposium*, Vol. 7, pp. 4474 – 4476.

Valenzuela, G. R. & Laing, M. B. (1970) Study of Doppler spectra of radar sea echo, *Journal of Geophysical Research* **75**, 551–563.

Walker, D. (2001*a*) Doppler modelling of radar sea clutter, *IEE Proceedings of Radar, Sonar and Navigation* **148**(2), 73–80.

Walker, D. (2001*b*) *Model and Characterisation of Radar Sea Clutter*, PhD thesis, University College London.

Ward, K. D., Tough, R. J. A. & Watts, S. (2006) *Sea Clutter: Scattering, the K-Distribution and Radar Performance*, The Institute of Engineering Technology.

Werle, B. O. (1995) Sea backscatter, spikes and wave group observations at low grazing angles, *in IEEE International Radar Conference*, pp. 187–195.

Wright, J. W. (1968) A new model for sea clutter, *IEEE Transactions on Antennas and Propagation* **16**(2), 217–223.

DEFENCE SCIENCE AND TECHNOLOGY ORGANISATION DOCUMENT CONTROL DATA				1. CAVEAT/PRIVACY MARKING
2. TITLE Sea-Spike Detection in High Grazing Angle X-band Sea-Clutter			3. SECURITY CLASSIFICATION Document (U) Title (U) Abstract (U)	
4. AUTHOR Luke Rosenberg			5. CORPORATE AUTHOR Defence Science and Technology Organisation PO Box 1500 Edinburgh, South Australia 5111, Australia	
6a. DSTO NUMBER DSTO–TR–2820	6b. AR NUMBER 015-571		6c. TYPE OF REPORT Technical Report	7. DOCUMENT DATE April 2012
8. FILE NUMBER 2012/1144904/1	9. TASK NUMBER AIR7000	10. TASK SPONSOR DGAD	11. No. OF PAGES 22	12. No. OF REFS 31
13. URL OF ELECTRONIC VERSION `http://www.dsto.defence.gov.au/publications/scientific.php`			14. RELEASE AUTHORITY Chief, Electronic Warfare and Radar Division	

15. SECONDARY RELEASE STATEMENT OF THIS DOCUMENT

Approved for Public Release

OVERSEAS ENQUIRIES OUTSIDE STATED LIMITATIONS SHOULD BE REFERRED THROUGH DOCUMENT EXCHANGE, PO BOX 1500, EDINBURGH, SOUTH AUSTRALIA 5111

16. DELIBERATE ANNOUNCEMENT

No Limitations

17. CITATION IN OTHER DOCUMENTS

No Limitations

18. DSTO RESEARCH LIBRARY THESAURUS

Sea-clutter, sea-spike detection, radar

19. ABSTRACT

Knowledge of radar sea-clutter phenomenology allows accurate models to be developed for assessing target detection performance. The majority of work in this area has been at low-grazing angles from clifftops or wave tanks and does not consider scattering in the high grazing angle region beyond 10°. To improve our understanding at high grazing angles 15° to 45°, the DSTO's Ingara airborne X-band fully polarimetric radar has been used to collect 12 days worth of sea-clutter data. This report focuses on understanding the characteristics of sea-spikes as they are often the cause of false detections in a radar processor. Using the Ingara data, a threshold is used to isolate these scatterers in the range/time domain with results verified against the KK probability distribution function. Detections due to discrete and persistent scattering are then isolated to provide more information regarding the underlying cause of sea-spikes and answer the question of whether Walker's three component mean Doppler spectrum model is suitable at high grazing angles.